Structure−Property Correlation in EEMAO Fabricated TiO$_2$−Al$_2$O$_3$ Nanocomposite Coatings

H. Niazi,[†,*] F. Golestani-Fard,[†] W. Wang,[‡] M. Shahmiri,[†] H. R. Zargar,[‡] A. Alfantazi,[‡] and R. Bayati[§]

[†]School of Metallurgy and Materials Engineering, Iran University of Science and Technology, Tehran, Iran
[‡]Department of Metals and Materials Engineering, University of British Columbia, Vancouver, British Columbia V6T 1Z4, Canada
[§]Intel Corporation, IMO-SC, SC2, Santa Clara, California 95054, United States

ABSTRACT: We grew TiO$_2$−Al$_2$O$_3$ nanocomposite coatings on titanium substrates by electrophoretic enhanced microarc oxidation (EEMAO) technique under several voltages and established a correlation between microstructure, surface hardness, and corrosion resistance of the coatings in sulfuric acid and sodium chloride solutions. Structural analysis revealed that the coatings contained anatase, rutile, alumina, and tialite phases. Formation kinetics of tialite phase was studied. It was found that increasing the voltage gives rise to a coarser morphology, i.e., larger pore size, and incorporation of more alumina nanoparticles into the layers. It is shown that surface hardness of the titanium substrates increased by a factor of 4 following EEMAO treatment. Corrosion resistance of titanium was enhanced significantly. Resistance against pitting corrosion was improved as well. We proposed a formation mechanism for the TiO$_2$−Al$_2$O$_3$ composite coatings at different voltages based on the chemical and electrochemical foundations.

KEYWORDS: EEMAO, TiO$_2$−Al$_2$O$_3$, nanocomposite, microhardness, corrosion

EEMAO Process
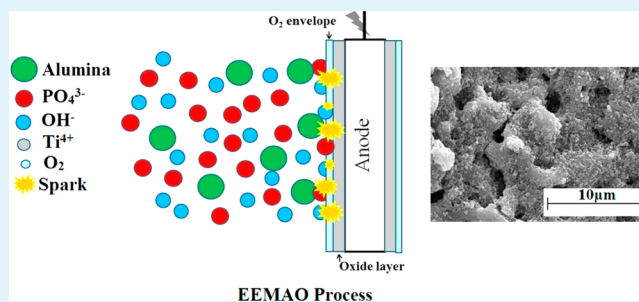
1. INTRODUCTION

Titanium and its alloys, by virtue of their high strength-to-weight ratio, favorable corrosion resistance in many environments, good mechanical behavior, and suitable biocompatibility have been used in many practical applications.[1] Aerospace,[1,2] marine,[3−5] biomedicine,[6,7] extractive metallurgy,[8] food processing, and oil and gas[9] are some examples of technological applications of titanium alloys. From a thermodynamic point of view and based on the relatively negative reversible potential of pure titanium on the electromotive force (EMF) series (E_o = −1.63 V versus natural hydrogen electrode), titanium is an active metal which chemically reacts with other species; that is, it oxidizes easily when exposed to the ambient atmosphere and aqueous and nonaqueous electrolytes[9,10] resulting in a spontaneous formation of a passive oxide film on the surface. The oxide film on the surface of titanium components has a low protecting efficiency and is easily destroyed, since it is very thin, i.e. 1.5−10 nm.[11−13] Moreover, passivated titanium shows a relatively poor corrosion resistance in contact with reducing acids, such as hydrochloric or sulfuric acids. In such environments, the passivating TiO$_2$ layer gets reduced to a soluble form of oxidized titanium and simply flakes off.[10,11] Besides, it should be taken into account that titanium-based components are often in tribological contact with other components under stationary or dynamic loading at different temperatures. Such a harsh condition can damage the thin native oxide film resulting in intensive interactions between the component and the counterface material or the environment. Removal of the passivating oxide layer and exposure of the bare titanium part to the surrounding environment give rise to a high friction or even seizure, galvanic corrosion, crevice corrosion, and corrosion embrittlement.[12,14,15] As a consequence, developing high performance and stable protective coatings on the titanium -based component seems to be a requirement to prevent these effects and improve performance and durability of the components.

One of the well-established and promising techniques to modify the surface of titanium alloys is oxidation, which can be performed by either heat treatment[16−19] or electrolytic anodizing.[1] Thermal oxidation technique is a thermochemical process, which is usually carried out in an oxygen containing atmosphere at 600−650 °C for tens of hours.[19] Increasing temperature accelerates the formation of a thick oxide layer,[18] but leads to debonding of the oxide layer.[16] Meanwhile, this process may be associated with the loss of bulk hardness and load bearing capacity of titanium alloys due to recrystallization.[17] Anodizing is also employed to fabricate relatively thick oxide coatings onto the titanium components. It is an electrochemical technique and is carried out for various purposes including decorative finishing, corrosion protection, and increasing the friction resistance.[1] Electrochemical oxidation produces anatase phase which shows lower corrosion resistance compare to rutile.[16] It is worth mentioning that titanium dioxide crystallizes in three primary polymorphs,

Table 1. Chemical Composition of the Substrate

	Al	V	Cr	Cu	Fe	Mn	Other	Ti
weight percent	0.25	≤0.05	≤0.01	≤0.02	0.04	0.10	0.11	rest

namely rutile, anatase, brookite. The former one is not stable and forms under extreme conditions with no practical application. Anatase is the metastable phase of titania and transforms into rutile upon heating. Rutile is the thermodynamically most stable phase of titania.

A modified version of the classic anodizing process is microarc oxidation (MAO). The main difference between these two techniques is the applied voltage which is far higher in MAO. Such high applied voltages change the growth mechanism of coatings drastically. It is a fast and low cost technique to produce oxide based layers on the surface of the valve metals, i.e., titanium,[20−23] aluminum,[24−26] magnesium,[27−31] and zirconium.[32] In this technique, anodic oxidation, thermal oxidation, and plasma-chemical mechanisms may be involved simultaneously.[33] This process is carried out at voltages higher than the breakdown voltage of the oxygen layer covering the substrate. The substrate is connected to positive pole of the power supply as anode. When the oxygen layer forms and enshrouds the substrate, electrical resistance of the electrochemical cell increases and the process continues provided that the applied voltage defeats the breakdown voltage of the gas layer. Applying such voltages leads to the formation of electrical discharges through which current could pass the gas layer. In fact, MAO is known by these electrical sparks.[15,34−38] It is established that electrical parameters,[13,39−43] chemical composition of the electrolyte,[12,14,15] and chemical composition of the substrate[44] determine all characteristics of the MAO-fabricated coatings. For instance, Al_2O_3−ZrO_2,[24,25] TiO_2−ZrO_2,[45] TiO_2−SiO_2,[46] and WO_3−TiO_2[21] composite coatings with different morphologies have been fabricated by altering the MAO parameters, particularly electrolyte composition and electrical variables. Furthermore, by adding insoluble nanoparticles into the electrolyte and using the electrophoretic forces, composite coatings such as ZrO_2−Hap−TiO_2,[7,47,48] Al_2O_3−Cr_2O_3,[49] Al_2O_3−CNT,[50] MgO−TiO_2,[51] MgO−ZrO_2,[52] TiO_2−ZrO_2,[53] and TiO_2−Al_2O_3[54] have been grown successfully. This technique which is called electrophoretic-enhanced microarc oxidation (EEMAO) takes the advantages of both MAO and electrophoretic deposition method. Details on the EEMAO technique can be found in our previous works.[47]

In this research, we grew TiO_2−Al_2O_3 composite coatings on the titanium substrates by EEMAO process under different voltages. Role of the applied voltage on microstructure, morphology, surface hardness, and corrosion resistance of the coatings was investigated. We show that surface hardness and corrosion resistance of the composite layers increased for coatings obtained at higher applied voltages. A structure−property paradigm was proposed based on the chemical and electrochemical foundations.

2. MATERIALS AND METHODS

Titanium substrates (commercially pure titanium grade 2) with dimensions of 30 mm × 15 mm and a thickness of 0.7 mm were used as anode. Chemical composition of the substrate is shown in Table 1. Prior to the layer synthesis, the substrates were mechanically polished by abrasive papers up to No. 1200 followed by washing in distilled water. Afterward, they were chemically etched in diluted HF solution (HF:H_2O = 1:20 vol %) at room temperature for 30 s, and then were washed in distilled water. The substrates were ultrasonically cleaned in acetone for 15 min and, finally, washed by distilled water. The electrolytes were prepared by dissolution of three sodium phosphate salt (TSP, $Na_3PO_4 \cdot 12H_2O$) with a concentration of 10 g L^{-1} in distilled water. Then, alumina nanoparticles (with an average size of 40 nm), with a concentration of 3 g L^{-1} were added to the TSP solution and dispersed by magnetic stirrer for 240 min at room temperature. The alumina powder was also ultrasonically dispersed at room temperature for 60 min. The pH of the suspensions was about 12. Because of the basic pH of the electrolyte, the alumina particles assume a negative charge in the solution. It should be noted that the point of zero charge (PZC) of pure alumina is pH 9. An ASTM 316 stainless steel cylindrical container, surrounding the substrates, was also used as cathode. Electrolyte temperature was fixed at 70 ± 3 °C employing a water circulating system. A homemade rectifier with a maximum output of 500 V/10 A was used as the current source. A series of samples were fabricated under varying voltages in a range of 250−450 V with intervals of +50 V under direct current (DC). Details of the sample preparation parameters are shown in Table 2.

Table 2. Details of the Growth Variables

sample code	applied voltage (V)	three sodium phosphate (g L^{-1})	alumina nanoparticles (g L^{-1})	growth time (min)	pH
3A25	250 ± 5				
3A30	300 ± 5				
3A35	350 ± 5	10	3	10	12
3A40	400 ± 5				
3A45	450 ± 5				

X-ray diffraction analysis (RigakuMultiflex, Cu−Kα radiation, λ = 1.54178 Å) was used to identify the structure of the synthesized coatings. Surface morphology and cross section of the samples was examined by scanning electron microscope (TESCAN, Vega II) equipped with energy dispersive spectroscopy (EDS) analyzer.

The Vickers microhardness test was done on the titanium substrates as well as the coatings by a MHV-1000Z-SCTMC tester applying a load of 10 g for 10 s. Average values of 5 separate measurements are reported.

The corrosion and electrochemical experiments were carried out in a solution of H_2SO_4 (40 g L^{-1}) and NaCl (40 g L^{-1}) and a water bath was used to keep the solution temperature at 55 ± 1 °C. Before each test, high purity argon gas was purged into the solutions to deaerate the solution for 30 min. In addition, argon was kept purging during the testing process to ensure the experiments were carried out in the deaerated condition. A water bath was used to keep the solution temperature at 55 ± 1 °C. The experimental setup was a conventional water-jacketed three-electrode cell with a graphite rod counter electrode and an Ag/AgCl ([KCl] = 4 M) reference electrode. The cell was made of glass with a capacity of 1200 mL, in which 1000 mL of solution was used for all tests. All potentials in this work are reported vs Ag/AgCl reference electrode. The exposed area of the test specimen was 1 cm^2 for all samples. All the electrochemical measurements were carried out by a Princeton Applied Research Versastat 4 potentiostat/galvanostat. The open circuit potential (OCP) measurements were performed for 1 h to monitor the variation of the OCP during the immersion process. The linear polarization resistance (LPR) tests were carried out with potential scan from −20 mV vs OCP to 20 mV vs OCP and a sweep rate of 0.167 mV/s. The cyclic potentiodynamic polarization (CPP) measurements were performed from −1 to 9.9 V vs Ag/AgCl with a scan rate of 10 mV/s. For cyclic polarization, the scan direction was reversed when the samples reached the anodic corrosion current of 100 mA and
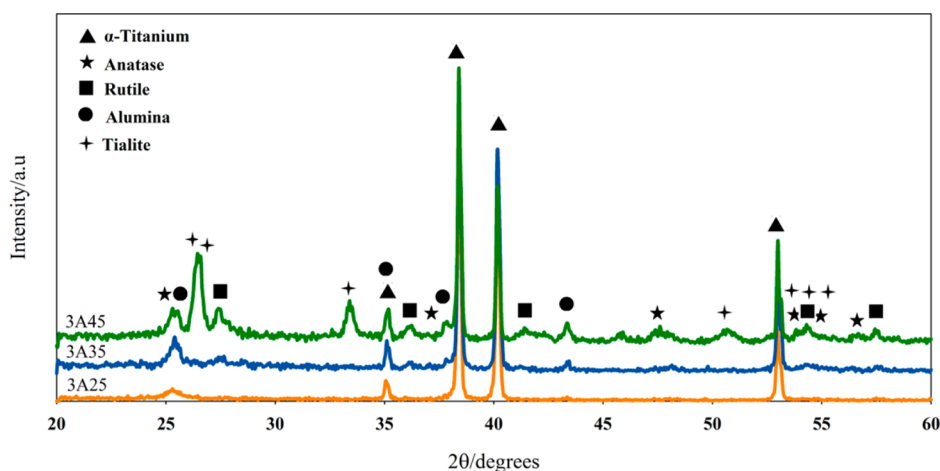
5539

dx.doi.org/10.1021/am405938n | ACS Appl. Mater. Interfaces 2014, 6, 5538−5547

Figure 1. XRD patterns of composite coatings fabricated under different voltages.

potential was scanned back. The electrochemical impedance spectroscopy (EIS) measurements were conducted with the amplitude of 10 mV at OCP in the frequency range of 10^5 to 0.05 Hz. All EIS data were analyzed using ZView software. Prior to all electrochemical measurements, the samples were immersed for 1 h in the test solution so that the electrode/solution interfaces reach a quasi-steady state. The reported results from LPR, CPP, and EIS tests are actually the average of three different measurements.

3. RESULTS AND DISCUSSION

3.1. Coating Phase Structure. XRD patterns, depicted in Figure 1, demonstrate that the coatings were composed of anatase, rutile, alumina, and tialite phases. As is seen, intensity of the characteristic peaks of the anatase phase increased with voltage. The mean current passing the electrochemical cell at various applied voltage were measured and the corresponding results are shown in Figure. 2. The mean current increased
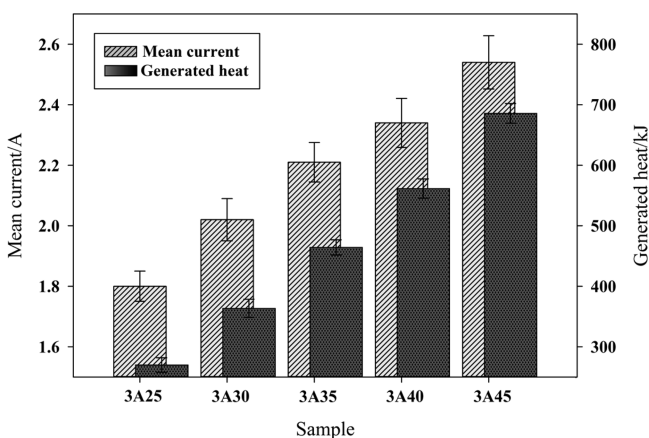

Figure 2. Mean current flow and generated heat for different samples.

from 1.81 to 2.54 A when the applied voltage changed from 250 to 450 V resulting in a thicker film due to the accelerated electrochemical reactions. Furthermore, the intensity of the XRD lines from the rutile and alumina phases changed at varying applied voltages. For instance, none of the characteristic peaks of rutile and alumina were observed in the XRD pattern taken from the sample, synthesized at 250 V, while these peaks appeared in the XRD pattern of the sample fabricated at 350 V. This means that thermal oxidation and electrophoretic deposition were not prevailing at low voltages, i.e., 250 V.

Generated heat on the anode surface was calculated through eq 1 and the results are shown in Figure 2.

$$Q = VIt \tag{1}$$

where V is electrical potential (V), I is current (A), t is time (s), and Q is the generated heat (J). According to Figure 2, the generated heat increases with the applied voltage, which leads to a phase transformation of anatase into rutile. It is worth mentioning that rutile is the thermodynamically stable state of titania at elevated temperatures.[34,35,51]

It should be also noted that the electrical sparks become stronger and more energetic at higher applied voltages giving rise to a local temperature and pressure as high as 1×10^3 to 1×10^4 K and 1×10^2 to 1×10^3 MPa, respectively.[27] Since the PZC of alumina is about 9, the alumina nanoparticles were negatively charged in the electrolyte; thus, they are affected by the electrophoretic forces between anode and cathode. As the electric field between anode and cathode was amplified at higher voltages, stronger electrophoretic forces were generated. This phenomenon resulted in alumina nanoparticles accelerating toward anode and, thus, increased alumina content in the growing layer.

The characteristic peaks of tialite were observed in the XRD pattern taken from the sample 3A45. Tialite forms through eq 2.[55] In fact, for this sample, generated heat and applied electrophoretic force satisfied the thermodynamic and kinetics conditions for the formation of tialite.

$$TiO_2 + Al_2O_3 \rightarrow TiAl_2O_5 \tag{2}$$

3.2. Coating Morphology. Figure 3 displays surface morphology of the composite coatings synthesized in an electrolyte containing 3 g L^{-1} alumina nanoparticles under different voltages where growth of porous structures is evident. It has been shown that the electric discharges are responsible for the formation of such porous structures. These electrical sparks initiate when the applied voltage is higher than the sparking critical voltage (V_{CS}). V_{CS} is the voltage before which no electrical spark is generated and no pore forms.[34] Figure 3 shows that the density of the micropores and pore size change with the applied voltage. It is worth mentioning that higher voltages cause electrical sparks with higher energies; as a result, larger pores appear on the surface at increased voltages. The density of the micropores initially increased, reached a maximum at 350 V, and decreased at higher voltages. At
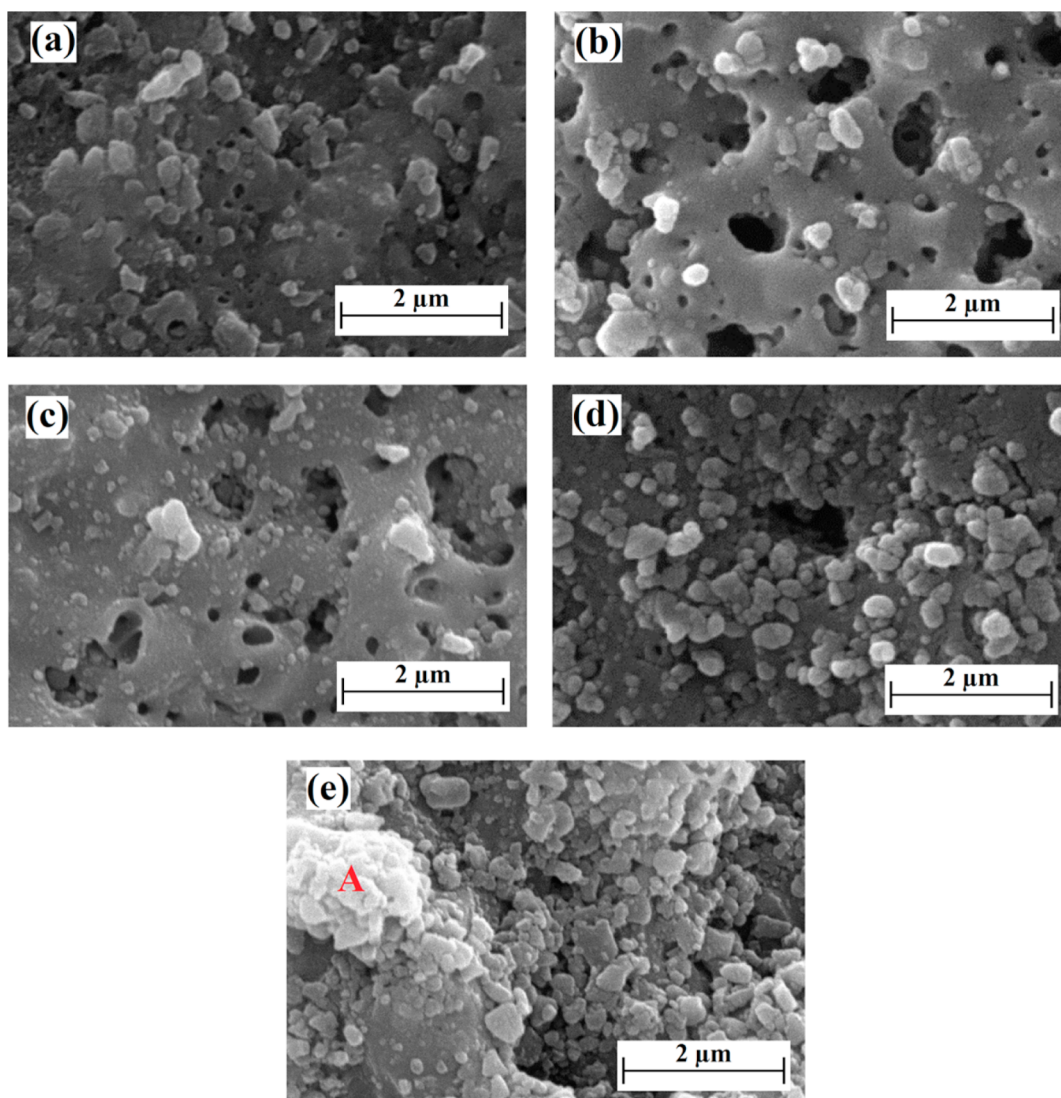
Figure 3. Surface morphology of the composite coatings grown at: (a) 250, (b) 300, (c) 350, (d) 400, and (e) 450 V.

voltages lower than 350 V, the voltage at the anode surface reached the breakdown voltage at limited sites; hence, few pores formed. As the applied voltage was raised, the number of sites at which the voltage reached breakdown voltage increased, and therefore, more pores formed. However, beyond this voltage, strong electron avalanches take place, giving rise to connecting the pores, already formed, and decreasing the pore density.[39,48,56,57]

Another feature of the micrographs shown in Figure 3 is the effect of voltage on the content of the particles accumulated on surface. Figure 4 displays the EDS elemental analysis of point A in Figure 3e. Considering the intense peak of aluminum, it is concluded that the bright particles on the surface might be alumina nanoparticles.

Figure 5 depicts cross-section SEM images of the composite layers synthesized under different voltages, which demonstrates that thicker layers grew at higher voltages.

According to Figure 5, at the voltage of 450 V, the thickness increased dramatically. This phenomenon can be explained by the incorporation of alumina nanoparticles. The aluminum content in the coatings was measured by EDS technique and the corresponding results are presented in Figure.6. The aluminum content can be considered as a criterion for
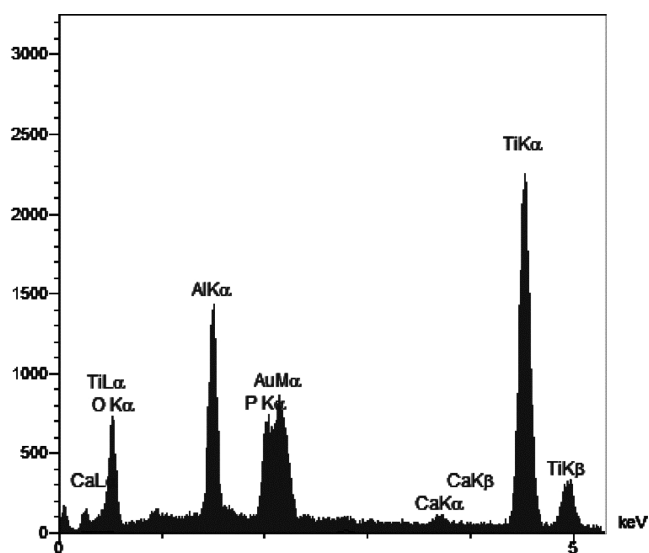

Figure 4. Elemental analysis of point A in Figure 3e.

evaluating nanoparticle content in the coatings. The sharp increases in the aluminum content of the coating, grown under
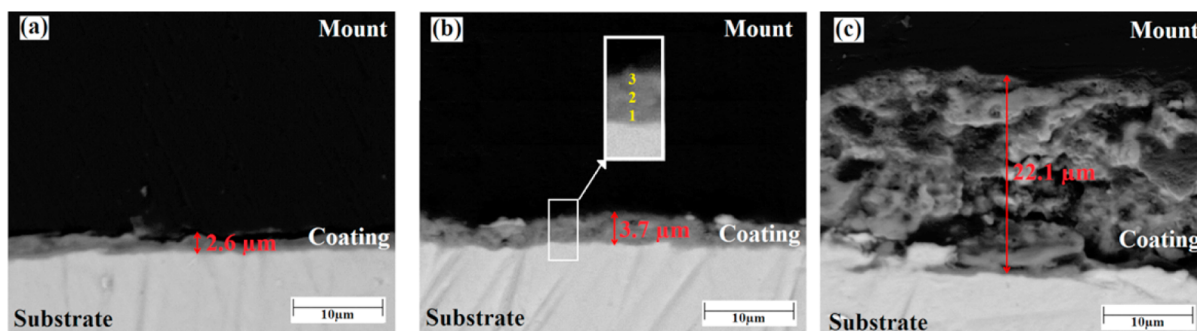
Figure 5. Cross-section images of the composite coatings fabricated under: (a) 250, (b) 350, and (c) 450 V.
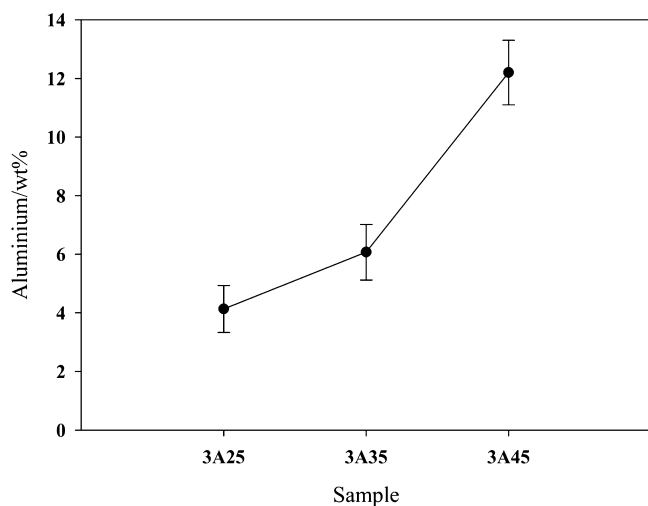

Figure 6. Aluminum weight percentage in the composite coatings.

the voltage of 450 V, shows that electrophoretic deposition occurred more effectively at this voltage which also increased coating thickness. This suggestion is in agreement with the model proposed by Malyshev et al.,[49] indicating that the thickness increases by the incorporation of particles. EDS analysis was performed at three different points across the cross section of the coatings to conform the incorporation of alumina naoporticles to the coatings. Figure 7 shows the aluminum concentration in depth of sample 3A35. The positions of the
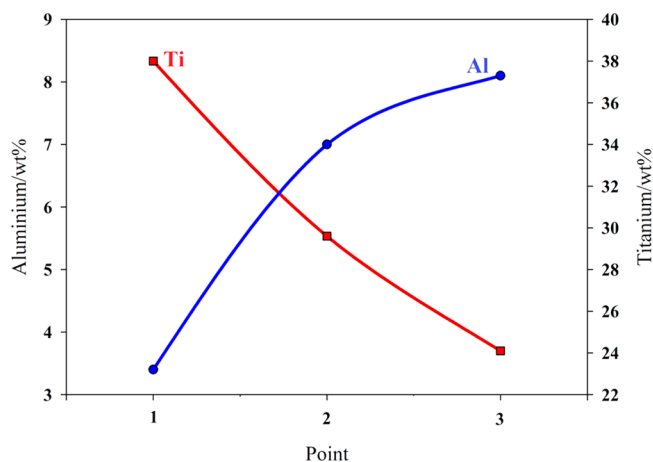

Figure 7. Weight percentage changes of Aluminum and Titanium across to the coating layer.

points, where EDS analysis was performed, can be found in the corresponding SEM image (Figure 5b). These results ascertain the incorporation of alumina nanoparticles in the bulk of the coatings.

3.3. Coatings Formation Mechanisms. Figure 8 illustrates a probable mechanism of EEMAO growth of
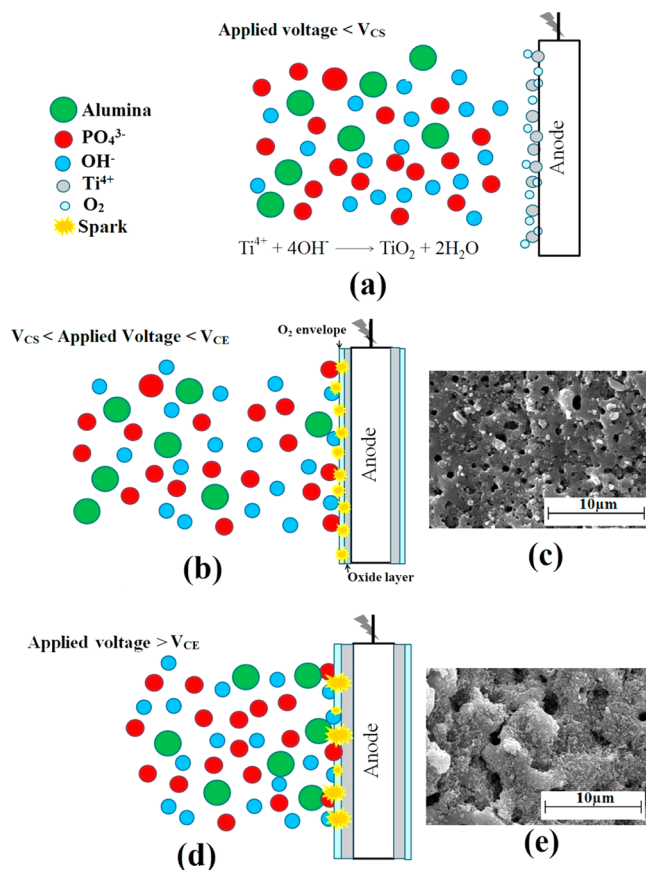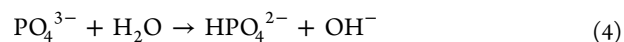

Figure 8. Schematic illustration of the EEMAO process.

titania-alumina composite coatings schematically. Because of the dissolution of sodium phosphate in water, OH^- ions are generated as shown below[56−58]

$$Na_3PO_4 \rightarrow 3Na^+ + PO_4^{3-} \tag{3}$$

$$PO_4^{3-} + H_2O \rightarrow HPO_4^{2-} + OH^- \tag{4}$$

When potential is applied to the electrochemical cell, an electric field is generated between anode and cathode and; as a result, anions move toward the positive pole (anode). On the

5542

dx.doi.org/10.1021/am405938n | ACS Appl. Mater. Interfaces 2014, 6, 5538−5547

other hand, Ti^{4+} ions are produced by anodic dissolution of the titanium substrates. On the surface of anode, TiO_2 forms through the following reaction

$$Ti^{4+} + 4OH^- \rightarrow TiO_2 + 2H_2O \qquad (5)$$
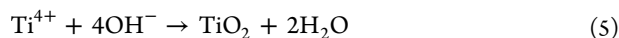
At the same time, large amount of O_2 bubbles form on the anode surface.[35] No electrical discharge is observed at this stage and the electrophoretic force is not strong enough to move alumina particles toward the anode surface. This stage is a prerequisite for EEMAO process and proceeds until the critical voltage at which the electrical sparks appear (Figure 8a). In fact, at the V_{CS}, TiO_2 thickness gets large enough, and together with O_2 bubbles forms a continuous envelope that acts as a barrier layer. An intense electric field forms across the barrier layer and sparks are locally initiated at the sites having lower electrical resistance. Because in Figure 3a a number of micropores are present, it can be concluded that the V_{CS} was equal to or less than 250 V. In this regard, two distinct formation mechanisms can be proposed on the basis of the applied voltages. When the applied voltage is higher than V_{CS} and lower than 350 V, tiny sparks form on the anode surface. The electrophoretic force applied on the nanoparticles at this stage is not sufficient for effective incorporation of alumina nanoparticles. In addition, the heat generated by both the electrical sparks and the electrical current passing through the electrochemical cell leads to a partial phase transformation of anatase to rutile. This process is depicted in Figure 8b which can be the dominant formation mechanism for 3A25, 3A30, and 3A35 samples. This suggestion is confirmed by the SEM micrograph taken from the 3A30 sample (Figure 8c), where a large number of fine micropores and smaller incorporation of nanoparticles are observed.

Applying voltages higher than 350 V leads to sparks with higher energy and larger size, as is delineated in Figure 8d. As discussed earlier, the mean current increased at higher voltages and, as a result, stronger sparks formed. This phenomenon generates fewer micropores with larger size.[39,48,56,57] In addition, the electrophoretic force is intensified at this stage, thus, the incorporation of alumina nanoparticles is enhanced. As a result, it can be suggested that there is a critical voltage for electrophoretic deposition (V_{CE}) which is about 350 V. The surface morphology of the sample 3A45 is shown in Figure 8e where the formation of a layer with large pores and large amount of alumina nanoparticles is evident. Moreover, at higher voltages, more heat is generated which enhances the anatase to rutile phase transformation. The formation of tialite also occurs because of the availability of enough alumina nanoparticles and more generated heat on the anode surface.

3.4. Microhardness Evaluation. Figure 9 depicts Vickers hardness values of the substrate and the composite layers grown under different voltages. As is seen, the surface hardness of the titanium substrate has increased following EEMAO processing. The formation of thick titania layers and incorporation of more alumina nanoparticles might be the reason behind the enhanced surface hardness at higher voltages. Besides, alumina nanoparticles could act as nucleation sites during the growth of the titania coatings. Therefore, a finer structure with enhanced hardness is obtained.[53,59]

3.5. Corrosion Behavior. Figure 10 shows the variation of open circuit potential (OCP) for CP-Ti and composite coatings during 1 h immersion in the deaerated solution at 55 °C. Results indicate that the OCP of CP-Ti decreased rapidly at the very initial immersion stage, which was caused by the rapid
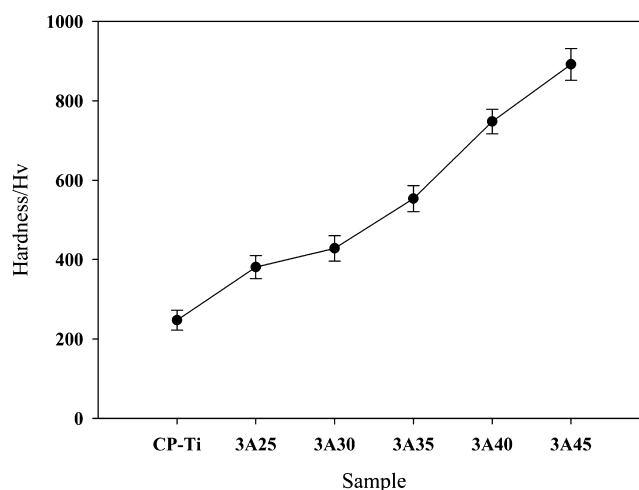

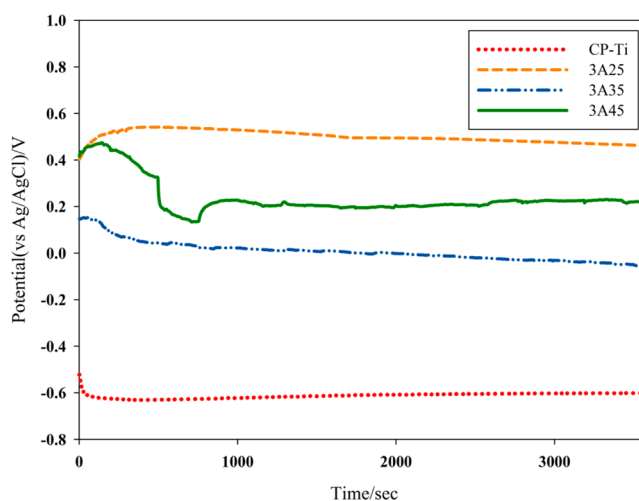**Figure 9.** Vickers hardness of the composite coatings.

Figure 10. Variation of OCP during the immersion process in a deaerated solution of 40 g L^{-1} H_2SO_4 + 40 g L^{-1} NaCl at 55 °C.

dissolution of the air-formed oxide film on Ti surface, suggested that the air-formed Ti oxide film is not stable in deaerated 40 g L^{-1} H_2SO_4 + 40 g L^{-1} NaCl solution at 55 °C. With longer immersion time, the OCP of Ti reached a quasi-steady state, indicating that the active dissolution of Ti metal into the solution.

According to Figure 10, EEMAO process made the electrode potential of CP-Ti move from negative to positive. In other words, preparation of ceramic coatings which contain anatase, rutile, alumina and tialite phases, that are more stable in corrosive environment, increased the OCP values.[11,44] It should be noted that the tests were conducted under deaerated condition, and as a result, the cathodic reaction for CP-Ti is as follows

$$2H^+ + 2e^- \leftrightarrow H_2 \qquad E° = -0.197 \text{ V vs Ag/AgCl} \qquad (6)$$
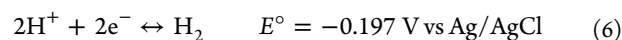
so, if the only cathodic reaction is the reduction of H^+, the OCP must be lower than −0.197 V, which is the case for CP-Ti in this experiment. However, the OCP of coated samples were higher than this value, and it might be concluded that some of the Ti or other metal ions have been reduced and served as the cathodic reactions, supporting the high OCP values in these deaerated solutions.

It can also be observed that OCP measures decreased with increasing the coating formation voltage. As mentioned in sections 3.2 and 3.3, coating formation voltage changed phase composition and microstructure of the coatings. It seems that larger porosities decreased OCP values. If the coating is porous, the small pores can be active sites for dissolution of the coating. However, in the case of 3A45 sample, tialite formation reduced the effects of micropores. Approximately constant OCP values for the coatings during the last 40 min of immersion suggest the stability of the films in the chosen solution.

Cyclic potentiodynamic polarization (CPP) curves of CP-Ti and coated samples are shown in Figure 11. EEMAO process
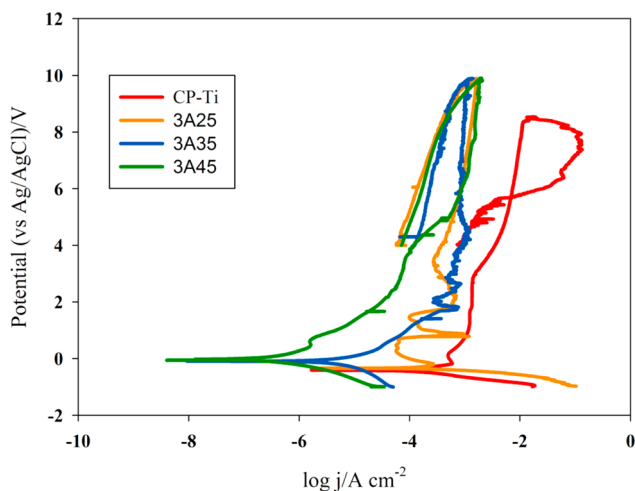

Figure 11. Cyclic potentiodynamic polarization curves of CP-Ti and coated samples in a deaerated solution of 40 g L^{-1} H$_2$SO$_4$ + 40 g L^{-1} NaCl at 55 °C.

moved the current density of CP-Ti to lower values. In other words, formation of coatings which contain electrical insulators phases such as anatase, rutile, alumina and tialite led to a decline in electrochemical tendency and restricted anodic reactions.[11,14,15] As is seen, current densities also reduced for coatings synthesized at higher applied voltage; for instance when the potential was lower than 5 V, the current density of 3A45 was significantly lower than 3A25 and 3A35. As shown before, coating thickness increased dramatically for the sample synthesized at 450 V. Thus, this thick coating reduced the charge-carrier mobility at the metal−electrolyte interface and restricted adsorbing of corrosive ions. Furthermore, the formation of tialite phase can also influence electrochemical reactions.[12,15]

The other feature of CPP curves is the movement of corrosion potential of the coated samples to more positive values in comparison with titanium substrate, due to the formation of more stable phases on the surface. In addition, corrosion potential of the coated samples increased for coatings prepared at higher voltages. Additionally, the positive hysteresis in CPP curve for titanium substrate shows low pitting resistance of CP-Ti. In fact pitting was not observed for CP-Ti when the potential was lower than 4 V. However, with the increase in the potential, pitting behavior initiated as shown in Figure 11. At the potential of 8 V the reverse scan was applied and the repassivation potential (E_{rp}) was observed around 5 V in this experiment. It is generally believed that pits will continue to grow when the potential is greater than E_{rp} and pits will not grow when potential is less than that. So in this case, pitting will

not occur on Ti surface when the potential is lower than 5 V.[60] In contrast to the titanium CPP curve, negative hysteresis was seen in CPP curves of coated samples. Negative hysteresis occurred when reverse scan current density was less than that for the forward scan. It also occurs when a damaged passive film repairs itself or pits do not initiate. Thus, in the case of coated samples, no pitting occurred in the potential range up to 10 V. Consequently, it can be concluded that EEMAO coatings provide excellent pitting resistance under experimental condition.

Obtained results from LPR test are reported at Table 3. According to Table 3, EEMAO process increased the

Table 3. Polarization Resistance of CP-Ti and Ti-Coatings in a Deaerated Solution of 40 g L^{-1} H$_2$SO$_4$ + 40 g L^{-1} NaCl at 55 °C Obtained from LPR Studies

sample	polarization resistance (kΩ cm^2)
CP- Ti	0.2 ± 0.1
3A25	48.7 ± 3.8
3A35	124.7 ± 4.6
3A45	873.7 ± 323.1

polarization resistance. It is obvious that corrosion rate decreased for samples obtained at higher voltages. In fact, anatase to rutile phase transformation and the increase in coating thickness are two possible reasons for this behavior. In addition, the higher corrosion resistance of 3A45 sample can be due to tialite formation. These results show good agreement with obtained data from CPP curves.

Figure 12 shows Nyquist plot of CP-Ti. Two loops are observed which can be attributed to dual layered structure of
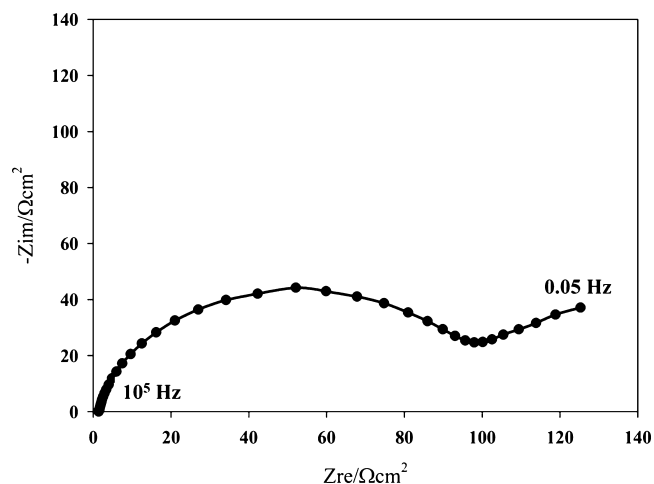

Figure 12. Nyquist plots of EIS measurements for CP-Ti in a deaerated solution of 40 g L^{-1} H$_2$SO$_4$ + 40 g L^{-1} NaCl at 55 °C.

the native oxide film which is composed of an inner and an outer part. The inner layer has a compact structure and forms across the metal-oxide interface. Passivation behavior of the oxide film and majority of the potential drop across the oxide film are due to this compact layer. The outer layer, because of its porous structure, has limited passivation characteristics.[10] Therefore, the bare titanium electrical equivalent circuit has to have two time constant, i.e., two loops.

Nyquist plot of the coated samples are shown in Figure 13. It is possible to compare corrosion resistance of coated samples
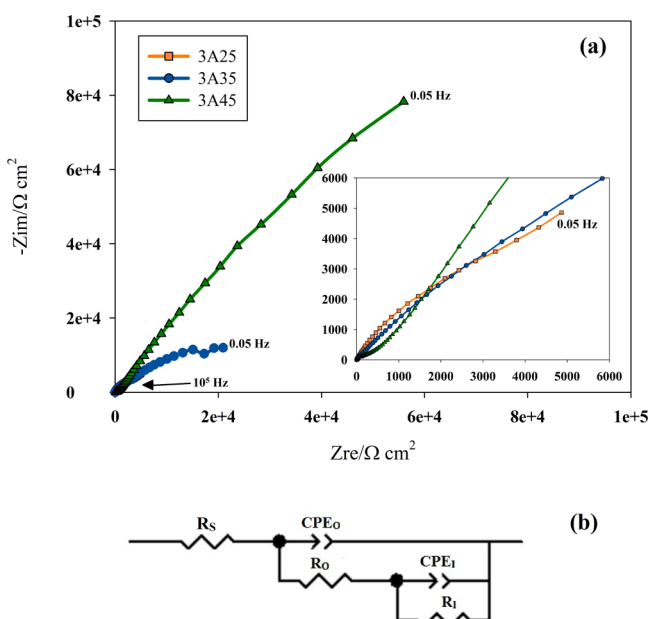
Figure 13. (a) Nyquist plots of EIS measurements for coated samples in a deaerated solution of 40 g L^{-1} H_2SO_4 + 40 g L^{-1} NaCl at 55 °C and (b) electrical equivalent circuit.

through diameter of the nyquist curves. The nyquist curves of samples with better corrosion resistance has greater diameter. Accordingly, corrosion resistances are in the order of 3A45 > 3A35 > 3A25.

The coatings that form by the EEMAO method also contain dual layer structures. The electrical sparks or plasma interactions with metal and electrolyte results in outer porous layer and the inner compact layer form by electrochemical reactions induced by applied voltage over the metal.[61,62] An electrical equivalent circuit which is shown in Figure 13b was used to simulate EIS data for titanium and coated samples.[41,52,62−65] In this equivalent electrical circuit, R_s is the solution resistance between the working electrode and the reference electrode, CPE_I (constant phase element) and R_I are representative of the capacitive and the resistive behavior of the internal compact layer, CPE_O and R_O signify the capacitive and the resistive behavior of the external porous layer of the dual layer oxide. The CPE is used to account for the nonuniform current distribution from the pure capacitive behavior and the deviation due to surface inconsistencies. CPE can be represented by

$$Z_{CPE} = 1/[T(jw)^n] \qquad (7)$$

Where T is the general admittance function with unit of F cm^{-2} $S^{(n-1)}$, ω is the angular frequency and n is a coefficient related to the dispersive behavior with values between 0 and 1. As the

value of n approaches 1, CPE behaves as a pure capacitor. The circuit elements are reported in Table 4. As it is presented in Table 4, the accuracy of simulations has been evaluated by chi-Squared factor which is about 1×10^{-4}.

As the simulation data show, the resistances of the impact inner layers (R_I) are greater than that of the outer porous layers (R_O). Thus, it can be concluded that R_I plays an important role in corrosion protection and determines overall corrosion resistance. Furthermore, according to obtained results, R_I values increased for samples obtained at higher voltages. In fact, first, increasing the applied voltage enhanced electrochemical oxidation which contributed to the circumstances under which the thickness of the inner layer increases. Second, according to Lee et al.,[52] nanoparticles fill micropores and as a result, porosity decreases across the outer layer and it can be assumed that the thickness of the inner layer increases. As mentioned before, incorporation of alumina nanoparticles increased dramatically in 3A45 sample, thus it can be another chief reason for its improved R_I. Overall, it can be concluded that, EEMAO method increases corrosion resistance of titanium in the corrosive media.

4. CONCLUSION

Titania-alumina nanocomposite coatings were synthesized successfully by EEMAO process, and the following results were obtained:

(1) The data obtained from XRD patterns proved the presence of anatase, rutile, alumina, and tialite phases. The amplified electrophoretic forces and increased generated heat at higher voltages enhance the incorporation of alumina nanoparticles and the transformation of anatase to rutile, respectively. These phenomena provide thermodynamic (heat) and kinetic conditions (alumina content) for the tialite formation in sample 3A45.

(2) The incorporation of more alumina nanoparticles, the formation of courser morphology, and the growth of thicker layers at higher voltages were confirmed by SEM studies.

(3) The microhardness of the layers was improved with the increase in the voltage.

(4) The coatings fabricated by EEMAO technique was stable in a deaerated solution of 40 g L^{-1} H_2SO_4 + 40 g L^{-1} NaCl at 55 °C . The corrosion resistance of Ti was significantly increased by the EEMAO coatings.

■ AUTHOR INFORMATION

Corresponding Author
*E-mail: niazi@metaleng.iust.ac.ir. Tel: +989126469415. Fax: +982177240291.

Notes
The authors declare no competing financial interest.

Table 4. Simulated EIS Results of Titanium and Composite Coatings after 1 h Immersion in a Deaerated Solution of 40 g L^{-1} H_2SO_4 + 40 g L^{-1} NaCl at 55 °C

sample code	R_S (Ω cm^2)	outer layer			internal layer			χ^2
		R (Ω cm^2)	T (F cm^{-2} S^{n-1})	n	R (Ω cm^2)	T (F cm^{-2} S^{n-1})	n	
CP-Ti	2	102	1.03×10^{-3}	0.89	62	5.70×10^{-2}	0.97	1.4×10^{-4}
3A25	5	5179	1.55×10^{-4}	0.73	10813	4.61×10^{-4}	0.91	8.8×10^{-4}
3A35	9	9232	3.75×10^{-5}	0.65	32280	2.14×10^{-5}	0.71	2.8×10^{-4}
3A45	7	798	6.71×10^{-6}	0.63	6.32×10^5	1.47×10^{-5}	0.69	8.7×10^{-4}

■ REFERENCES

(1) Sharma, A. K. Anodizing Titanium for Space Applications. *Thin Solid Films* 1992, *208*, 48−54.

(2) Moiseev, V. N. Titanium in Russia. *Met. Sci. Heat Treat.* 2005, *47*, 371−376.

(3) Gorynin, I. V. Titanium Alloys for Marine Application. *Mater. Sci. Eng., A* 1999, *263*, 112−116.

(4) Williams, W. L. Development of Structural Titanium Alloys for Marine Applications. *Ocean. Eng.* 1969, *1*, 375−383.

(5) Gurrappa, I. Characterization of Titanium Alloy Ti-6Al-4V for Chemical, Marine and Industrial Applications. *Mater. Charact.* 2003, *51*, 131−139.

(6) Liu, X.; Chu, P. K.; Ding, C. Surface Modification of Titanium, Titanium Alloys, and Related Materials for Biomedical Applications. *Mater. Sci. Eng., R* 2004, *47*, 49−121.

(7) Samanipour, F.; Bayati, M. R.; Golestani-Fard, F.; Zargar, H. R.; Mirhabibi, A. R; Shoaei-Rad, V.; Abbasi, S. Innovative Fabrication of ZrO_2−HAp−TiO_2 Nano/Micro-Structured Composites through MAO/EPD Combined Method. *Mater. Lett.* 2011, *65*, 926−928.

(8) Vaughan, J.; Alfantazi, A. Corrosion of Titanium and Its Alloys in Sulfuric Acid in the Presence of Chlorides. *J. Electrochem. Soc.* 2006, *153*, B6−B12.

(9) Komotori, J.; Lee, B. J.; Dong, H.; Dearnley, P. A. Corrosion Response of Surface Engineered Titanium Alloys Damaged by Prior Abrasion. *Wear* 2001, *251*, 1239−1249.

(10) *ASM Handbook: Corrosion: Fundamentals, Testing, and Protection*, 9th ed.; Carmer, S. D.; Convino, B. S., Eds.; ASM International: Materials Park, OH, 2003, Chapter 4, p 703−711.

(11) Yao, Z.; Jiang, Z.; Wu, X.; Sun, X.; Wu, Z. Effects of Ceramic Coating by Micro-Plasma Oxidation on the Corrosion Resistance of Ti−6Al−4V alloy. *Surf. Coat. Technol.* 2005, *200*, 2445−2450.

(12) Shokouhfar, M.; Dehghanian, C.; Baradaran, A. Preparation of Ceramic Coating on Ti Substrate by Plasma Electrolytic Oxidation in Different Electrolytes and Evaluation of Its Corrosion Resistance. *Appl. Surf. Sci.* 2011, *257*, 2617−2624.

(13) Kuromoto, N. K.; Simão, R. A.; Soares, G. A. Titanium Oxide Films Produced on Commercially Pure Titanium by Anodic Oxidation with Different Voltages. *Mater. Charact.* 2007, *58*, 114−121.

(14) Shokouhfar, M.; Dehghanian, C.; Montazeri, M.; Baradaran, A. Preparation of Ceramic Coating on Ti Substrate by Plasma Electrolytic Oxidation in Different Electrolytes and Evaluation of Its Corrosion Resistance: Part II. *Appl. Surf. Sci.* 2012, *258*, 2416−2423.

(15) Yerokhin, A. L.; Nie, X.; Leyland, A.; Matthews, A. Characterization of Oxide Films Produced by Plasma Electrolytic Oxidation of a Ti−6Al−4V alloy. *Surf. Coat. Technol.* 2000, *130*, 195−206.

(16) Krishna, D. S. R.; Brama, Y. L.; Sun, Y. Thick Rutile Layer on Titanium for Tribological Applications. *Tribol. Int.* 2007, *40*, 329−334.

(17) Güçlü, F. M.; Çimenoğlu, H.; Kayalı, E. S. The Recrystallization and Thermal Oxidation Behavior of CP-Titanium. *Mater. Sci. Eng., C* 2006, *26*, 1367−1372.

(18) Güleryüz, H.; Çimenoğlu, H. Effect of Thermal Oxidation on Corrosion and Corrosion−Wear Behaviour of a Ti−6Al−4V Alloy. *Biomaterials* 2004, *25*, 3325−3333.

(19) Dong, H.; Bell, T. Enhanced Wear Resistance of Titanium Surfaces by a New Thermal Oxidation Treatment. *Wear* 2000, *238*, 131−137.

(20) Bayati, M. R.; Golestani-Fard, F.; Moshfegh, A. Z.; Molaei, R. In Situ Derivation of Sulfur Activated TiO_2 Nano Porous Layers through Pulse-Micro Arc Oxidation Technology. *Mater. Res. Bull.* 2011, *46*, 1642−1647.

(21) Bayati, M. R.; Golestani-Fard, F.; Moshfegh, A. Z.; Molaei, R. A Photocatalytic Approach in Micro Arc Oxidation of WO_3−TiO_2 Nano Porous Semiconductors under Pulse Current. *Mater. Chem. Phys.* 2011, *128*, 427−432.

(22) Matykina, E.; Monfort, F.; Berkani, A.; Skeldon, P.; Thompson, G. E.; Gough, J. Characterization of Spark-Anodized Titanium for Biomedical Applications. *J. Electrochem. Soc.* 2007, *154*, C279−C285.

(23) Yao, Z.; Jia, F.; Tian, S.; Li, C.; Jiang, Z.; Bai, X. Microporous Ni-Doped TiO_2 Film Photocatalyst by Plasma Electrolytic Oxidation. *ACS Appl. Mater. Interfaces* 2010, *2*, 2617−2622.

(24) Shoaei-Rad, V.; Bayati, M. R.; Zargar, H. R.; Javadpour, J.; Golestani-Fard, F. In Situ Growth of ZrO_2−Al_2O_3 Nano-Crystalline Ceramic Coatings via Micro Arc Oxidation of Aluminum Substrates. *Mater. Res. Bull.* 2012, *47*, 1494−1499.

(25) Shoaei-Rad, V.; Bayati, M. R.; Golestani-Fard, F.; Zargar, H. R.; Javadpour, J. Fabrication of ZrO_2−Al_2O_3 Hybrid Nano-Porous Layers through Micro Arc Oxidation Process. *Mater. Lett.* 2011, *65*, 1835−1838.

(26) Monfort, F.; Berkani, A.; Matykina, E.; Skeldon, P.; Thompson, G. E.; Habazaki, H.; Shimizu, K. A Tracer Study of Oxide Growth During Spark Anodizing of Aluminum. *J. Electrochem. Soc.* 2005, *152*, C382−C387.

(27) Seyfoori, A.; Mirdamadi, S.; Khavandi, A.; Raufi, Z. S. Biodegradation Behavior of Micro-Arc Oxidized AZ31 Magnesium Alloys Formed in Two Different Electrolytes. *Appl. Surf. Sci.* 2012, *261*, 92−100.

(28) Ryu, H. S.; Mun, S. J.; Lim, T. S.; Kim, H. C.; Shin, K. S.; Hong, S. H. Microstructure Evolution During Plasma Electrolytic Oxidation and Its Effects on the Electrochemical Properties of AZ91D Mg Alloy. *J. Electrochem. Soc.* 2011, *158*, C266−C273.

(29) Lim, T. S.; Ryu, H. S.; Hong, S. H. Plasma Electrolytic Oxidation/Cerium Conversion Composite Coatings for the Improved Corrosion Protection of AZ31 Mg Alloys. *J. Electrochem. Soc.* 2013, *160*, C77−C82.

(30) Li, Z.; Yuan, Y.; Sun, P.; Jing, X. Ceramic Coatings of LA141 Alloy Formed by Plasma Electrolytic Oxidation for Corrosion Protection. *ACS Appl. Mater. Interfaces* 2011, *3*, 3682−3690.

(31) Wu, X.; Su, P.; Jiang, Z.; Meng, S. Influences of Current Density on Tribological Characteristics of Ceramic Coatings on ZK60 Mg Alloy by Plasma Electrolytic Oxidation. *ACS Appl. Mater. Interfaces* 2010, *2*, 808−812.

(32) Pauporté, T.; Finne, J.; Kahn-Harari, A.; Lincot, D. Growth by Plasma Electrolysis of Zirconium Oxide Films in the Micrometer range. *Surf. Coat. Technol.* 2005, *199*, 213−219.

(33) Matykina, E.; Arrabal, R.; Monfort, F.; Skeldon, P.; Thompson, G. E. Incorporation of Zirconia into Coatings Formed by DC Plasma Electrolytic Oxidation of Aluminium in Nanoparticle Suspensions. *Appl. Surf. Sci.* 2008, *255*, 2830−2839.

(34) Bayati, M. R.; Golestani-Fard, F.; Moshfegh, A. Z. How Photocatalytic Activity of the MAO-Grown TiO_2 Nano/Micro-Porous Films is Influenced by Growth Parameters? *Appl. Surf. Sci.* 2010, *256*, 4253−4259.

(35) Yerokhin, A. L.; Nie, X.; Leyland, A.; Matthews, A.; Dowey, S. J. Plasma Electrolysis for Surface Engineering. *Surf. Coat. Technol.* 1999, *122*, 73−93.

(36) Yerokhin, A. L.; Leyland, A.; Matthews, A. Kinetic Aspects of Aluminium Titanate layer Formation on Titanium Alloys by Plasma Electrolytic Oxidation. *Appl. Surf. Sci.* 2002, *200*, 172−184.

(37) Gupta, P.; Tenhundfeld, G.; Daigle, E. O.; Ryabkov, D. Electrolytic Plasma Technology: Science and Engineering—An Overview. *Surf. Coat. Technol.* 2007, *201*, 8746−8760.

(38) Khorasanian, M.; Dehghan, A.; Shariat, M. H.; Bahrololoom, M. E.; Javadpour, S. Microstructure and Wear resistance of Oxide Coatings on Ti−6Al−4V Produced by Plasma Electrolytic Oxidation in an Inexpensive Electrolyte. *Surf. Coat. Technol.* 2011, *206*, 1495−1502.

(39) Bayati, M. R.; Moshfegh, A. Z.; Golestani-Fard, F. Effect of Electrical Parameters on Morphology, Chemical Composition, and Photoactivity of the Nano-Porous Titania Layers Synthesized by Pulse-Microarc Oxidation. *Electrochim. Acta* 2010, *55*, 2760−2766.

(40) Huang, P.; Wang, F.; Xu, K.; Han, Y. Mechanical Properties of Titania Prepared by Plasma Electrolytic Oxidation at Different Voltages. *Surf. Coat. Technol.* 2007, *201*, 5168−5171.

(41) Montazeri, M.; Dehghanian, C.; Shokouhfar, M.; Baradaran, A. Investigation of the Voltage and Time Effects on the Formation of Hydroxyapatite-Containing Titania Prepared by Plasma Electrolytic

Oxidation on Ti−6Al−4V Alloy and Its Corrosion Behavior. *Appl. Surf. Sci.* **2011**, *257*, 7268−7275.

(42) Hussein, R. O.; Zhang, P.; Nie, X.; Xia, Y.; Northwood, D. O. The Effect of Current Mode and Discharge Type on the Corrosion Resistance of Plasma Electrolytic Oxidation (PEO) Coated Magnesium Alloy AJ62. *Surf. Coat. Technol.* **2011**, *206*, 1990−1997.

(43) Yao, Z.; Xu, Y.; Jiang, Z.; Wang, F. Effects of Cathode Pulse at low Frequency on the Structure and Composition of Plasma Electrolytic Oxidation Ceramic Coatings. *J. Alloys Compd.* **2009**, *488*, 273−278.

(44) Song, H. J.; Kim, M. K.; Jung, G. C.; Vang, M. S.; Park, Y. J. The Effects of Spark Anodizing Treatment of Pure Titanium Metals and Titanium Alloys on Corrosion Characteristics. *Surf. Coat. Technol.* **2007**, *201*, 8738−8745.

(45) Yao, Z.; Jiang, Y.; Jiang, Z.; Wang, F.; Wu, Z. Preparation and Structure of Ceramic Coatings Containing Zirconium Oxide on Ti Alloy by Plasma Electrolytic Oxidation. *J. Mater. Process. Technol.* **2008**, *205*, 303−307.

(46) Wang, Y. M.; Jiang, B. L.; Lei, T. Q.; Guo, L. X. Microarc Oxidation Coatings Formed on Ti6Al4V in Na₂SiO₃ System Solution: Microstructure, Mechanical and Tribological Properties. *Surf. Coat. Technol.* **2006**, *201*, 82−89.

(47) Samanipour, F.; Bayati, M. R.; Golestani-Fard, F.; Zargar, H. R.; Troczynski, T.; Mirhabibi, A. R. An Innovative Technique to Simply Fabricate ZrO₂−HA−TiO₂ Nanostructured Layers. *Colloids Surf., B* **2011**, *86*, 14−20.

(48) Samanipour, F.; Bayati, M. R.; Zargar, H. R.; Golestani-Fard, F.; Troczynski, T.; Taheri, M. Electrophoretic Enhanced Micro Arc Oxidation of ZrO₂−HAp−TiO₂ Nanostructured Porous Layers. *J. Alloys Compd.* **2011**, *509*, 9351−9355.

(49) Malyshev, V. N.; Zorin, K. M. Features of Microarc Oxidation Coatings Formation Technology in Slurry Electrolytes. *Appl. Surf. Sci.* **2007**, *254*, 1511−1516.

(50) Lee, K. M.; Jo, J. O.; Lee, E. S.; Yoo, B.; Shin, D. H. Incorporation of Carbon Nanotubes into Oxide Layer on 7075 Al Alloy by Plasma Electrolytic Oxidation. *J. Electrochem. Soc.* **2011**, *158*, C325−C328.

(51) Liang, J.; Hu, L.; Hao, J. Preparation and Characterization of Oxide Films Containing Crystalline TiO₂ on Magnesium Alloy by Plasma Electrolytic Oxidation. *Electrochim. Acta* **2007**, *52*, 4836−4840.

(52) Lee, K. M.; Shin, K. R.; Namgung, S.; Yoo, B.; Shin, D. H. Electrochemical Response of ZrO₂-Incorporated Oxide Layer on AZ91 Mg Alloy Processed by Plasma Electrolytic Oxidation. *Surf. Coat. Technol.* **2011**, *205*, 3779−3784.

(53) Yousefipour, K.; Akbari, A.; Bayati, M. R. The Effect of EEMAO Processing on Surface Mechanical Properties of the TiO₂-ZrO₂ Nanostructured Composite Coatings. *Ceram. Int.* **2013**, *39*, 7809−7815.

(54) Aliofkhazraei, M.; Rouhaghdam, A. S. Wear and Coating Removal Mechanism of Alumina/Titania Nanocomposite Layer Fabricated by Plasma Electrolysis. *Surf. Coat. Technol.* **2011**, *205*, S57−S62.

(55) Bayati, M. R.; Zargar, H. R.; Talimian, A.; Ziaee, A.; Molaei, R. Characterization of Al₂O₃−TiO₂ Nano Porous Solar Absorbers Derived via MAO/Sol-Gel Hybrid Process. *Surf. Coat. Technol.* **2010**, *205*, 2483−2489.

(56) Bayati, M. R.; Golestani-Fard, F.; Moshfegh, A. Z. Visible Photodecomposition of Methylene Blue over Micro Arc Oxidized WO₃−Loaded TiO₂ Nano-Porous Layers. *Appl. Catal., A* **2010**, *382*, 322−331.

(57) Bayati, M. R.; Moshfegh, A. Z.; Golestani-Fard, F. In Situ Growth of Vanadia−Titania Nano/Micro-Porous Layers with Enhanced Photocatalytic Performance by Micro-Arc Oxidation. *Electrochim. Acta* **2010**, *55*, 3093−3102.

(58) Wan, L.; Li, J. F.; Feng, J. Y.; Sun, W.; Mao, Z. Q. Anatase TiO₂ Films with 2.2 eV Band Gap Prepared by Micro-Arc Oxidation. *Mater. Sci. Eng., B* **2007**, *139*, 216−220.

(59) Yari, S.; Dehghanian, C. Deposition and Characterization of Nanocrystalline and Amorphous Ni−W Coatings with Embedded Alumina Nanoparticles. *Ceram. Int.* **2013**, *39*, 7759−7766.

(60) Tait, W. S.; *An Introduction of Electrochemical Corrosion Testing for Practicing Engineers and Scientists*, 1st ed.; PairODocs Publication: Racine, WI, 1994; P 67.

(61) Kuhn, A. Plasma Anodizing of Magnesium Alloys. *Met. Finish.* **2003**, *101*, 44−50.

(62) Ghasemi, A.; Raja, V. S.; Blawert, C.; Dietzel, W.; Kainer, K. U. Study of the Structure and Corrosion Behavior of PEO Coatings on AM50 Magnesium Alloy by Electrochemical Impedance Spectroscopy. *Surf. Coat. Technol.* **2008**, *202*, 3513−3518.

(63) Wen, L.; Wang, Y. M.; Liu, Y.; Zhou, Y.; Guo, L. X.; Ouyang, J. H.; Jia, D. C. EIS Study of a Self-Repairing Microarc Oxidation Coating. *Corros. Sci.* **2011**, *53*, 618−623.

(64) Shi, X.; Xu, L.; Wang, Q. Porous TiO₂ Film Prepared by Micro-Arc Oxidation and Its Electrochemical Behaviors in Hank's Solution. *Surf. Coat. Technol.* **2010**, *205*, 1730−1735.

(65) Venkateswarlu, k.; Rameshbabu, N.; Sreekanth, D.; Sandhyarani, M.; Bose, A. C.; Muthupandi, V.; Subramanian, S. Role of Electrolyte Chemistry on Electronic and in Vitro Electrochemical Properties of Micro-Arc Oxidized Titania Films on Cp Ti. *Electrochim. Acta* **2013**, *105*, 468−480.